



Comparison of scanning aerosol LIDAR and *in-situ* measurements of aerosol physical properties and boundary layer heights

Hengheng Zhang¹, Christian Rolf², Ralf Tillmann³, Christian Wesolek³, Frank Gunther Wienhold⁴, Thomas Leisner¹, and Harald Saathoff¹

¹Institute of Meteorology and Climate Research, Karlsruhe Institute of Technology, Eggenstein-Leopoldshafen, Karlsruhe, Germany

²Institute of Energy and Climate Research - Stratosphere (IEK-7), Research Center Jülich, Wilhelm-Johnen-Straße, Jülich, Germany

³Institute of Energy and Climate Research - Troposphere (IEK-8), Research Center Jülich, Wilhelm-Johnen-Straße, Jülich, Germany

⁴Institute for Atmospheric and Climate Science, ETH Zürich, Universitätstrasse 16, Zürich, Switzerland

Correspondence: Hengheng Zhang (hengheng.zhang@kit.edu) and Harald Saathoff (Harald.Saathoff@kit.edu)

Abstract. The spatial-temporal distribution of aerosol particles in the atmosphere has a great impact on radiative transfer, clouds, and air quality. Modern remote sensing methods as well as airborne *in-situ* measurements by unmanned aerial vehicles (UAV) or balloons are suitable tools to improve our understanding of the role of aerosol particles in the atmosphere. To validate the measurement capabilities of three relatively new measurement systems and to bridge the gaps that are often encountered between remote sensing and *in-situ* observation as well as to investigate aerosol particles in and above the boundary layer, we conducted two measurement campaigns and collected a comprehensive dataset employing a scanning aerosol LIDAR, a balloon-borne radiosonde with the Compact Optical Backscatter Aerosol Detector (COBALD), an optical particle counter (OPC) on a UAV, as well as a comprehensive set of ground-based instruments. The extinction coefficients calculated from near-ground-level aerosol size distributions measured *in-situ* are well correlated with those retrieved from LIDAR measurements with a slope of 1.037 ± 0.015 and a Pearson correlation coefficient of 0.878, respectively. Vertical profiles measured by an OPC-N3 on a UAV show similar vertical particle distributions and boundary layer heights as LIDAR measurements. However, the sensor, OPC-N3, shows a larger variability in aerosol backscatter coefficient measurements with a Pearson correlation coefficient of only 0.241. In contrast, the COBALD data from a balloon flight are well correlated with LIDAR-derived backscatter data from the near ground level up to the stratosphere with a slope of 1.063 ± 0.016 and a Pearson correlation coefficient of 0.925, respectively. This consistency between LIDAR and COBALD data reflects a good data quality of both methods and proves that LIDAR can provide reliable and spatial distributions of aerosol particles with high spatial and temporal resolutions. This study shows that the scanning LIDAR has the capability to retrieve backscatter coefficients near ground level (from 25 m to 50 m above ground level) when it conducts horizontal measurement which isn't possible for vertically pointing LIDAR. These near-ground-level retrievals compare well with ground-level *in-situ* measurements. In addition, *in-situ* measurements on the balloon and UAV validated scanning LIDAR retrievals within and above the boundary layer. The scanning aerosol LIDAR allows us to measure aerosol particle distributions and profiles from the ground level to the stratosphere with an accuracy equal or better than *in-situ* measurements and with a similar spatial resolution.



1 Introduction

The large varieties of aerosol spatial-temporal distributions in the atmosphere cause large uncertainties in radiative forcing globally (Ramanathan et al., 2001) and these uncertainties have a great impact on climate change (Stocker, 2014). The distributions and evolution of aerosol are related to the emission of aerosols (Grythe et al., 2014; Tegen and Schepanski, 2018; Hamilton et al., 2022) and their loss pathway (Poreh and Cermak, 1964; Cheng et al., 2011; Xiang et al., 2019; Xue et al., 2022). In addition, another important factor affecting radiative forcing is aerosol optical properties (e.g. single scatter albedo (SSA), LIDAR ratio, scatter and absorption coefficients) (Alam et al., 2011; Romshoo et al., 2021), which also have large varieties for different types of aerosols (Lesins et al., 2002; Floutsi et al., 2022).

Many methods have been used to measure the spatial-temporal distribution and aerosol optical parameters regionally and globally. One of the most successful instruments for this purpose is the Moderate Resolution Imaging Spectroradiometer (MODIS) on Terra and Aqua satellites (Filonchik and Hurynovich, 2020; Qin et al., 2021). MODIS can provide column-integrated optical parameters like aerosol optical depth (AOD), Ångström exponent (AE), and single scatter albedo (SSA) to study the optical properties of mineral dust (Kaufman et al., 2005; Ginoux et al., 2012), urban aerosol (More et al., 2013; Munchak et al., 2013), forest fire smoke (MAE, 2009; Huesca et al., 2009) etc. Another successful satellite mission is the Cloud-Aerosol LIDAR and Infrared Pathfinder Satellite Observations (CALIPSO). CALIPSO combines an active LIDAR instrument with passive infrared and visible imagers to probe the vertical structure and properties of thin clouds and aerosols over the globe (Winker et al., 2009; Wang et al., 2021; Salehi et al., 2021).

In addition to these satellite missions, ground-based remote sensing methods are used to investigate aerosol optical properties (Kotthaus et al., 2023). Over the last decades, many ground-based observation networks were established to investigate aerosol properties regionally and globally. For example, the AERONET (AERosol RObotic NETwork) project is a federation of ground-based remote sensing aerosol networks that provides globally distributed observations of spectral aerosol optical depth (AOD), inversion products, and precipitation water in diverse aerosol regimes (Holben et al., 1998; Prasad and Singh, 2007; Mielonen et al., 2009). The Micro-Pulse LIDAR Network (MPLNET) is a federated network of Micro-Pulse LIDAR (MPL) systems designed to measure aerosol and cloud vertical structure, and boundary layer heights (Welton et al., 2006; Lolli et al., 2018). The European Aerosol Research LIDAR Network (EARLINET) is a multi-wavelength LIDAR network designed to create a quantitative, comprehensive, and statistically significant database for the horizontal, vertical, and temporal distribution of aerosols on a continental scale (Pappalardo et al., 2014a; Marinou et al., 2017).

In-situ measurements can also help us better understand aerosol optical properties. The most common instruments are the nephelometer and aethalometer, which can measure the wavelength-dependent optical parameters like scatter and absorption coefficients of aerosol particles (Anderson et al., 1996; Drinovec et al., 2015). The aerosol optical parameters are determined by particle size distribution, particle shape, and complex refractive index (Bohren and Huffman, 2008; Yao et al., 2022). The size distribution can be measured by different kinds of particle sizers like Scanning Mobility Particle Sizer (SMPS), Optical Particle Counter (OPC), and Aerodynamic Particle Sizer (APS). The aerosol complex refractive index is related to the aerosol chemical composition which can be measured by aerosol mass spectrometry. For decades, these *in-situ* aerosol characterization



instruments not only provided valuable datasets at ground level (Huang et al., 2019; Jiang et al., 2022) but also were deployed on aircraft, balloons, and unmanned aerial vehicles to get vertical profiles of aerosol parameters (Bahreini et al., 2003; Zhen et al., 2018; Brunamonti et al., 2021).

60 LIDAR is a powerful tool to measure the spatial distribution and optical parameters of aerosol (Böckmann et al., 2004; Matthias et al., 2004). Although many results have reported aerosol measurements by LIDAR (Matthias and Bösenberg, 2002; Pappalardo et al., 2014b; Hofer et al., 2020; Ceolato and Berg, 2021), there are fewer reports on comparison of *in-situ* measurement with LIDAR measurement to quantify uncertainties of LIDAR retrievals (Düsing et al., 2018; Xiafukaiti et al., 2020; Düsing et al., 2018). In addition, most vertical pointing LIDAR systems have overlap gap between the detector's field of view and

65 the laser beam from tens to around one thousand meters, which makes it difficult to get valid measurement near the surface (Wandinger and Ansmann, 2002) to compare with ground level *in-situ* measurements. However, scanning LIDAR can conduct horizontal measurements allowing to get vertical profiles of aerosol particles and boundary layer structure near the ground level (Althausen et al., 2000). In addition, scanning aerosol LIDAR can also determine LIDAR ratios to reduce the uncertainties in the LIDAR retrievals (Fernald, 1984; Zhang et al., 2022).

70 In recent years, vertical profiles of aerosol are also investigated more and more by Unmanned Aerial Vehicles (UAV) and LIDAR. For example, Liu et al. (2020) used the UAVs and LIDAR to study the vertical distribution of PM_{2.5} and interactions with the atmospheric boundary layer during the development of heavy haze pollution. Ferrero et al. (2019) compared the backscatter coefficient retrieved from LIDAR with that calculated from aerosol size distributions measured by OPC on tethered balloons in the Arctic to study the role of aerosol chemistry and dust composition in a closure experiment. Zhang et al. (2021)

75 compared boundary layer heights retrieved from aerosol LIDAR and tethered balloon measurements in semi-arid regions. Liu et al. (2021) found that wind shear generating turbulence reshaped the vertical profiles of parameters such as potential temperature (θ) and PM_{2.5} in the nocturnal boundary layer, which was the key factor leading to the development of entrainment at nighttime. Reineman et al. (2016) used ship-launched fixed-Wing UAVs to measure the marine atmospheric boundary layer and ocean surface processes. In addition, the vertical profiles of atmospheric parameters related to aerosol process such as temperature

80 (Zarco-Tejada et al., 2012), relative humidity (Spiess et al., 2007), wind (Spiess et al., 2007) and ozone concentration (Guimarães et al., 2019) are also obtained from UAV flights.

However, to our best knowledge, so far no dedicated comparison of scanning LIDAR measurement with *in-situ* observation has been performed over a wide altitude range. Therefore, we compared datasets on aerosol spatial-temporal distributions and evolutions combining remote sensing and *in-situ* measurements. Two field campaigns were conducted employing a scanning

85 aerosol LIDAR, a radiosonde with a backscatter sensor, an OPC on a UAV, and a comprehensive set of ground-level instruments. The first field campaign was conducted in downtown Stuttgart to compare LIDAR retrievals with ground level *in-situ* measurements. The second field campaign was done at the Jülich research center to compare LIDAR retrievals with OPC measurements on a UAV and a COBALD backscatter sensor on a radiosonde. The aim of this work is to compare the different methods in aerosol measurements, to validate scanning LIDAR retrievals, to discuss the uncertainties of the different methods

90 and the boundary layer evolutions from LIDAR and UAV retrievals.



2 Methods

Two field campaigns were conducted in downtown Stuttgart and at Jülich research center to compare scanning aerosol LIDAR measurements with different *in-situ* measurements. The first field campaign was conducted from February 5th to March 5th, 2018 in downtown Stuttgart (9.2024° E 48.7986° N, 247 m above sea level) employing a mobile container and a scanning aerosol LIDAR on the roof of the container. The ground-level *in-situ* measurements deployed in this mobile container provided aerosol particle size distributions, aerosol chemical composition, and meteorological information (Huang et al., 2019). The second field campaign was conducted from July 5th to 12th, 2018 at Jülich research center (6.4131° E, 50.9084° N, 110 m above sea level) employing a scanning aerosol LIDAR, a COBALD sensor hosted by a Vaisala RS41-SGP radiosonde, and an OPC on UAV. The scanning LIDAR called KASCAL used in these two field campaigns was developed by Raymetrics (LR111-ESS-D200, Raymetrics Inc.). A UAV (eBee, senseFly) carrying one OPC (OPC-N3, Alphasense Inc.), weather sensors and Global Positioning System (GPS) sensors provided altitude-dependent particle size distribution and also meteorological information above the Jülich research center. In addition, atmospheric parameters like pressure, temperature, relative humidity and wind information from the ground to 30 km above Jülich research center were gathered by a GPS-equipped radiosonde onboard a balloon that carried COBALD to measure altitude-dependent *in-situ* backscatter coefficients at two wavelengths (455 nm & 940 nm) (Brunamonti et al., 2021). The measurements during this work indicated that the backscatter was dominated by smaller particles with low depolarisation ratios so that it seemed justified to use a spherical model to represent these aerosol particles (Khlebtsov et al., 2005; Moroz, 2009; Wang et al., 2023). Hence, a Mie code (Leinonen, 2016) was used to calculate extinction coefficients and backscatter coefficients from aerosol size distributions for comparison with the LIDAR retrieval.

2.1 Scanning aerosol LIDAR

The 3D scanning LIDAR (KASCAL) used in the above two field campaigns has an emission wavelength of 355 nm and is equipped with elastic, depolarization, and vibrational Raman channels, hence allowing to retrieve extinction coefficients, backscatter coefficients, and depolarization ratios. The laser pulse energy and repetition frequency are 32.1 mJ and 20 Hz, respectively. The laser head, 200 mm telescope, and LIDAR signal detection units are mounted on a rotating platform allowing zenith angles from -7° to 90° and azimuth angles from 0° to 360°. This LIDAR works automatically, time-controlled, and continuously via software developed by Raymetrics. Detailed information can be found at <https://www.raymetrics.com/product/3d-scanning-LIDAR>, last access: 8 March 2021 (Avdikos, 2015; Zhang et al., 2022). During the first field campaign in downtown Stuttgart, the LIDAR conducted zenith scans with an elevation angle from 90° to 5° in steps of 5°. The measurements at 5° were used over a range representative of an altitude of 25-50 m to compare with ground-level *in-situ* measurements (3.7 m above ground level). It is assumed that these values are comparable within the mixing layer. During the second field campaign at Jülich research center, the LIDAR conducted zenith scans during UAV launch and the measurements at all elevation angles were used to get vertical profiles of aerosols from ground level up to the free troposphere to compare with an OPC measurement on the UAV. In addition, the LIDAR also conducted vertical pointing measurements in the night of July 12th, 2018 at Jülich research center to compare the vertical profiles of backscatter coefficients from LIDAR retrievals and COBALD measurement



on board of a radiosonde.

- 125 For the data analysis and calibration of the LIDAR system, we followed the quality standards of the European Aerosol Research
LIDAR Network (EARLINET) (Freudenthaler, 2016). For data analysis of zenith scans, we determine the vertical backscatter
coefficient profiles using the Klett-Fernald method (Fernald, 1984; Klett, 1985). And these vertical profiles of aerosol
backscatter coefficients was used as the reference values for other observation angles. In addition, the measured temperatures
and pressures from UAVs and balloons were used to calculate the molecular backscatter coefficients which can be used in
130 LIDAR retrievals.

The atmospheric boundary layer height determined from LIDAR by using the Haar wavelet transform (HWT) method is defined
as

$$z_{HWT} = \max[w_f(a, b)] = \max \frac{1}{a} \int_{z_{min}}^{z_{max}} X(z) H\left(\frac{z-b}{a}\right) dz \quad (1)$$

- In which w_f is the covariance transform value, $X(z)$ is the range corrected LIDAR signal defined as $X(z) = P(z) * z^2$, and
135 $H\left(\frac{z-b}{a}\right)$ is the Harr wavelet function as defined as followed:

$$H\left(\frac{z-b}{a}\right) = \begin{cases} 1 & b - \frac{a}{2} \leq z \leq b \\ -1 & b \leq z \leq b + \frac{a}{2} \\ 0 & \text{elsewhere} \end{cases} \quad (2)$$

The dilation a was tested and set to be 75 m for this work. z_{min} and z_{max} are the lower and upper heights for the LIDAR signal
profile, respectively. In addition, the boundary layer height was also retrieved from vertical profile of potential temperature by
using gradient method. (Seidel et al., 2010; Li et al., 2021).

140 2.2 Ground-level *in-situ* measurements in downtown Stuttgart

- The ground-level *in-situ* instruments were deployed in a mobile container that was deployed in a parks downtown Stuttgart.
Ambient temperature, relative humidity, wind direction, wind speed, global radiation, pressure, and precipitation data were
measured by a meteorological sensor (WS700, Lufft GmbH). Trace gases (O_3 , CO_2 , NO_2 , SO_2) were measured with the
gas monitors (Environment S.A). Particle number concentrations were recorded with two CPCs (CPC 3774, 3022, TSI Inc.).
145 Particle size distributions were measured with SMPS (DMA: TSI 3080, TSI Inc; CPC: CPC3022, TSI Inc), and OPC (Fidas200,
Palas, Inc). The OPC (Fidas200, Palas, Inc.) continuously measured particles in the size range of 0.18 - 18 μm . The OPC
used Lorenz-Mie theory to determine the particle number size distribution and this size distribution can be used to calculate
extinction coefficients via a Mie code (Leinonen, 2016). In this experiment, Fidas200 was operated with a flow rate of 5 L/min
and with a time resolution of 1 s.
- 150 Figure 1 shows the workflow in deriving the aerosol extinction coefficients from Mie calculations based on *in-situ* aerosol
characterisation instruments. The aerosol sizer (e.g. OPC) can provide dry aerosol particle size distribution, which can be
converted to the ambient aerosol size distributions by using hygroscopic growth factors (κ) calculated from aerosol chemical



155 composition using the ISORROPIA II thermodynamic equilibrium model (Fountoukis and Nenes, 2007). The aerosol chemical composition was measured by HR-TOF-AMS (Aerodyne Inc.). Most aerosol particles are constrained and well-mixed within the boundary layer and the aerosol complex refractive index remains almost constant (Raut and Chazette, 2008). Although, the sun photometer is integrating over the whole vertical column, the relatively high aerosol concentrations in the boundary layer dominate (Li et al., 2017). Therefore, it seems justified to use the aerosol complex refractive index derived from a nearby sun photometer (CE-318). Hence, we used the aerosol complex refractive index derived from a nearby sun photometer (CE-318). With ambient aerosol size distribution and complex refractive index, optical parameters (e.g. extinction coefficients) were calculated to compare with LIDAR retrievals.

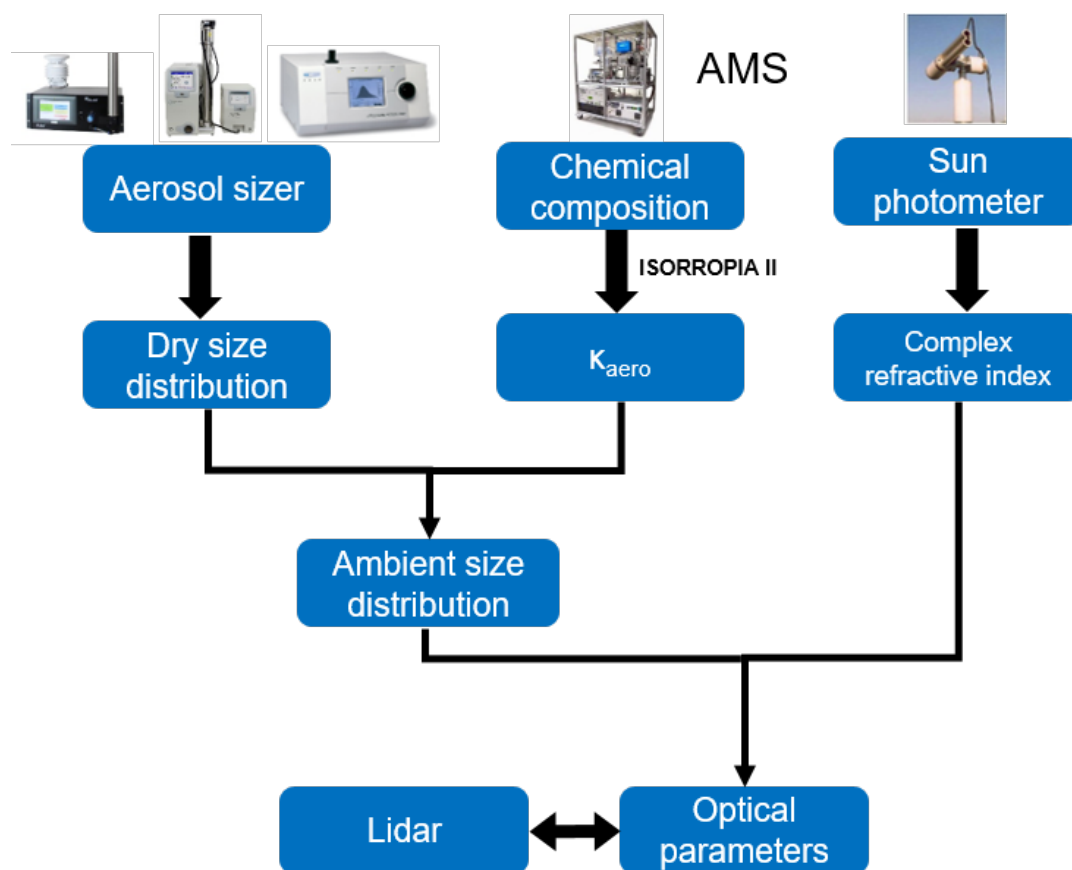


Figure 1. Process flow in deriving aerosol extinction coefficients from Mie calculation and parameters used in Mie calculations. κ_{aero} is the composition dependent hygroscopicity growth factor.



2.3 UAV and balloon-borne measurements at Research Center Jülich

Data of an OPC (OPC-N3, Alphasense, Inc) on a UAV and a COBALD backscatter sensor (Institute for Atmospheric and Climate Science, ETH Zurich) on a balloon were collected at Jülich research center in July 2018. The UAV used in this field campaign is a fixed-wing drone (eBee, senseFly) which is operated by the Institute of Energy and Climate Research - Tropo-
165 sphere (IEK-8). Its payload is 320 g at a total weight of 750 g with the highest observation altitude of approximately 1200 m above ground level. The ascent and descent velocity of this UAV was around 3.2 m/s. The measurement sensors were mounted inside the UAV. The size distributions were measured in real-time with a time resolution of 1.6 s by OPC-N3. Additionally, atmospheric parameters such as air temperature, air pressure, relative humidity, wind speed, and wind direction were measured with a temporal resolution of 1 s. The UAV was launched 5 times during the morning from 7:00 to 10:00 on July 9th to measure
170 the boundary layer dynamics in the early morning and was launched 7 times from 03:50 to 16:30 on July 12th to measure the boundary layer transition from nocturnal boundary layer to the mixing layer. The detailed UAV flights information can be found in Table 1.

Table 1. Time, altitude, and duration of UAV flights for the experiments on July 9th and July 12th, 2018.

Flight number	Date	Minimum altitude (m a.s.l.)	Maximum altitude (m a.s.l.)	Duration (s)
2018070901	2018.07.09 07:39	90.9	1246.5	709.5
2018070902	2018.07.09 07:48	92.4	1244.8	705.1
2018070903	2018.07.09 08:10	90.9	1243.8	711.7
2018070904	2018.07.09 08:29	89.5	1235.5	691.6
2018070905	2018.07.09 09:34	93.1	1752	1105.5
2018071201	2018.07.12 04:16	91.4	1247.1	701.3
2018071202	2018.07.12 04:31	94.8	1246.1	721.7
2018071203	2018.07.12 07:09	92.7	1246.5	719.6
2018071204	2018.07.12 07:33	93.2	1240.9	717.8
2018071205	2018.07.12 09:44	98.6	1253.7	722.3
2018071206	2018.07.12 14:30	92.8	1248.9	721.3
2018071207	2018.07.12 16:30	92.9	1240.2	716.5

Besides, a radiosonde balloon which was operated by the Institute of Energy and Climate Research - Stratosphere (IEK-7) measured the atmospheric parameters from ground to 25 km altitude. COBALD was part of a CFH / ECC ozone / RS41 payload to
175 provide the backscatter coefficients as well as air temperature, air pressure, relative humidity, and wind with the temporal and spatial resolution being 1s and around 5 m vertically.

The COBALD is a lightweight (500 g) aerosol backscatter detector for balloon-borne measurements developed at the Institute for Atmospheric and Climate Science (ETH Zürich), based on the original approach by Rosen and Kjöme (1991). Two light-emitting diodes (LEDs) as light sources and a photodiode detector with a FOV of 6° provide high-precision *in-situ*



180 measurements of aerosol backscatter at wavelengths of 455 nm (blue visible) and 940 nm (infrared). COBALD has been originally developed for the observation of high-altitude clouds, such as cirrus (Brabec et al., 2012; Cirisan et al., 2014) and polar stratospheric clouds (Engel et al., 2014), while recently it was proven able to detect and characterize aerosol layers in the upper troposphere–lower stratosphere (Vernier et al., 2015, 2018; Brunamonti et al., 2018, 2021). In this work, we compared COBALD measurements with scanning aerosol LIDAR measurements for validating LIDAR retrievals and investigating the vertical distribution of aerosols. A summary of sensors used on UAV and balloon flights is shown in Table 2.

Table 2. Summary of sensors used on on UAV and balloon flights.

Measurement	Instrument	Manufacturer	sample flow (lpm)	Time resolution	Mode of operation
UAV					
Particle size distribution (0.35 - 40 μ m)	OPC-N3	Alphasense	5.5	1.6 s	24 size bin
T, RH	ChipCap2 sensore	Telaire		1s	
Pressure, wind speed & direction	eBee sensors	AgEagle Aerial Systems Inc.		1 s	
Lat, lon,				1 s	
Balloon					
Backscatter ratio (455 nm & 940 nm)	COBALD	IAC (ETH, Zürich)		1 s	
Ozone	Electrochemical concentration cell (ECC)	JOSIE (Smit et al., 2007)		1s	
Water vapor	Cryogenic frostpoint hygrometer (CFH)	EnSci (Vömel et al., 2007; Vömel et al., 2016)		1s	
Temperature	Vaisala RS41-SGP	Vaisala		1s	
Altitude, lat, lon & horizontal wind				1s	



3 Results and Discussion

3.1 Comparison of LIDAR data with ground level *in-situ* measurements

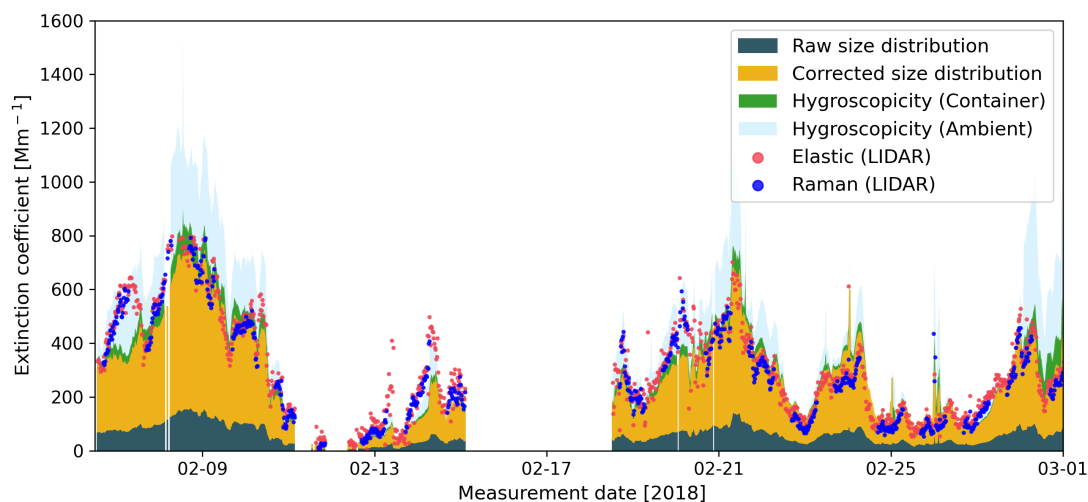


Figure 2. Time series of ground-level extinction coefficients retrieved from LIDAR measurements (both elastic and Raman methods), Mie calculation based on OPC raw size distribution as well as size distribution corrected by counting efficiency and hygroscopic effect from February 5th to March 5th, 2018 in downtown Stuttgart.

The comparison of LIDAR retrievals with ground-level aerosol sizer data was conducted during a field campaign from February 5th to March 5th, 2018 in downtown Stuttgart. In this campaign, the aerosol LIDAR did zenith scans with an elevation angle from 90 ° to 5° in steps of 5°. The nearly horizontal measurement at 5° allows to retrieve extinction coefficients near ground level (from 25 m to 50 m above ground level) by using short-range LIDAR data (ranges: 285 m to 570 m) that can be compared with the ground-level *in situ* measurements (sampled 3.7 m above ground level). The ground-level *in-situ* aerosol sizer, Fidas200, measured the aerosol size distributions which were used to calculate the aerosol extinction coefficients via Mie code. Figure 2 shows the extinction coefficients retrieved from LIDAR measurements and from Mie calculations based on aerosol size distribution (labeled as "Raw size distribution"). The extinction coefficients obtained from LIDAR were both retrieved from the slope and Raman retrieval methods (Seidel et al., 2010; Ansmann et al., 1992). In the slope and Raman retrieval methods, a linear regression was used and the correlation coefficients of linear regressions are 0.99 ± 0.05 and 0.99 ± 0.06 for slope and Raman retrieval methods, respectively. This is also an indication for a rather homogeneous distribution of the aerosol particles within the altitude range from 25 to 50 m corresponding to a range between 285 and 570 m. This figure shows that the raw extinction coefficients from Mie calculations are systematically lower than those from LIDAR retrievals by a factor of 4.70 ± 1.49 . The reason for this phenomenon is that the Fidas200 underestimates the particle number by a factor of 2-10 at a diameter between 0.25 μm and 0.5 μm when compared with SMPS data as shown in Figure S1. The left side of Figure S1



shows the number size distribution from Fidas200 and the merged size distribution from SMPS and APS measurements. From this figure, we can see that Fidas200 underestimated particle number size distributions at a diameter between 0.25 μm and 0.5 μm when compared with the merged size distribution (called "loss effect"). The right plot of this figure shows the accumulated extinction coefficients calculated from Mie based on those two size distributions, which shows that the underestimation of particle numbers from 0.25 μm to 0.5 μm causes the modelled extinction from the Fidas200 size distributions to be lower than that modelled from merged size distribution by a factor of around 4. Hence, we conclude that the underestimation of particle number from 0.25 μm to 0.5 μm is one of the main reasons for the underestimation of extinction coefficients based on OPC data alone.

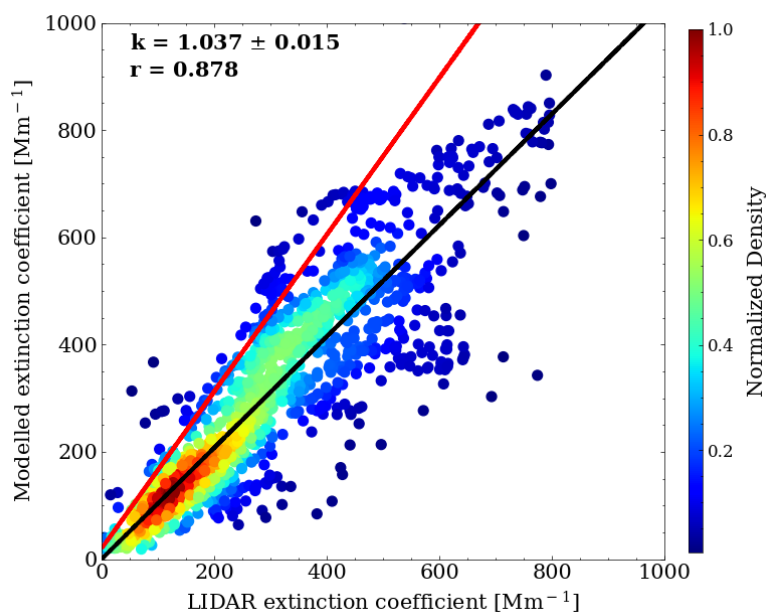


Figure 3. Correlation of extinction coefficients from LIDAR retrieval and Mie calculation from February 5th to March 5th, 2018 in Stuttgart. The relative humidity used in the model is container indoor relative humidity and the black line is the regression fitting curve of them. The red line is the regression fitting curve between the LIDAR-derived extinction coefficients and those from Mie calculation by using ambient relative humidity.

The systematic underestimation of aerosol particle number from 0.25 μm to 0.5 μm allows for calculating a counting efficiency curve as shown in Figure S2. Then the calculated counting efficiency curve was applied to the Fidas200 size distribution to get a corrected aerosol size distribution. This corrected size distribution is used to calculate the corrected extinction coefficients via
215 Mie calculation. The time series of the corrected extinction coefficients calculated from the corrected size distribution is shown in Figure 2. The orange area indicates the extinction coefficients due to the underestimation of aerosol particle number from 0.25 μm to 0.5 μm . After taking into account the particle number underestimation, the modelled extinction coefficient shows



good agreement with LIDAR retrievals. Although good agreement between *in-situ* and LIDAR measurements, the aerosol hygroscopic growth effect is still not considered. The modelled extinction coefficients contributed by aerosol hygroscopic growth are labeled as "hygroscopicity (container)" and "hygroscopicity (Ambient)" in Figure 2, representing the relative humidity used in the model are container indoor relative humidity and ambient relative humidity, respectively. The correlation plot between the extinction coefficient for container indoor relative humidity and the LIDAR-derived extinction coefficient is shown in Figure 3, which shows a slope and a Pearson correlation coefficient of 1.037 ± 0.015 and 0.878, respectively. The dashed line in this figure is the regression fitting curve between the LIDAR-derived extinction coefficients and those from Mie calculation by using ambient relative humidity, which shows a slope and a Pearson correlation coefficient of 1.463 ± 0.025 and 0.845, respectively. As shown in these two figures, the extinction coefficients retrieved from LIDAR measurement show a similar trend for both extinction coefficients but shows better agreement with the one calculated based on the container indoor relative humidity. The reason for a better agreement based on the indoor relative humidity instead of the outdoor ambient relative humidity is due to the fact that the aerosol particles lost their water partly inside the container but did not reach equilibrium within the 3 s residence time in the sampling line. Please note, that there was no dryer in the sampling line and the impact of the relative humidity correction on our comparison is much smaller than the correction of the size measurements. From the fraction of extinction coefficients shown in Figure 2, we can determine that the main reason for causing extinction coefficient inconsistency between *in-situ* measurement and LIDAR retrieval is the undercounting by the OPC. The relatively good agreement of the extinction coefficients after our reasonable corrections reflects the reliability of our methods and the good quality of the LIDAR retrievals.

3.2 Comparison of LIDAR data with *in-situ* measurements on a UAV

The comparison of LIDAR and UAV measurements was conducted for two days, on July 9th and July 12th, 2018 to study the vertical distribution of aerosols and the boundary layer structure. The sky was almost free of clouds during UAV flights on July 9th while it was affected by clouds within the boundary layer on July 12nd. Figure 4 shows the time series of backscatter coefficients and boundary layer retrieved from LIDAR measurement (pink squares) as well as boundary layer height (a.s.l. - above sea level) obtained from ERA5 dataset (white dashed line) and potential temperatures obtained from UAV measurements (white solid line) on July 9th, 2018. This figure shows that the boundary layer height retrieved from the LIDAR measurement is consistent with the boundary layer height from the UAV measurement (the maximum gradient of potential temperature) which both show an increasing trend of the boundary layer during the morning of this day. In addition, the boundary layer from ERA5 also shows a similar trend as the observations but overestimates boundary layer height, especially during daytime. A possible reason for this overestimation is that the existence of clouds during daytime reduced solar radiation and a low value of solar radiation caused a shallow boundary layer at this time. Figure 4 also shows a stable nocturnal boundary layer and a residual layer during nighttime measured by scanning aerosol LIDAR. The low and stable boundary at night time can suppress the dispersion of aerosol near the surface. Hence, the backscatter coefficients within the boundary layer are maximum (highest aerosol concentration) during the morning rush hour due to the combined effect of the shallow boundary layer and local anthropogenic emissions. After sunrise, the convection became stronger, which caused an increase of the boundary layer height and dilution of

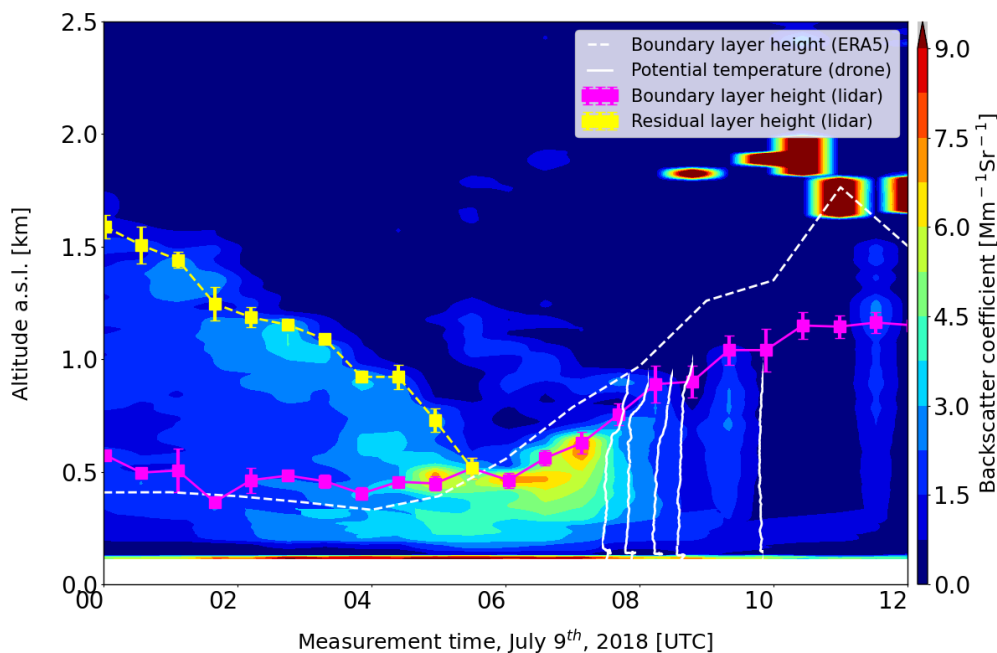


Figure 4. Time series of backscatter coefficients (contour), boundary layer height (pink squares) and residual layer retrieved (yellow squares) from scanning LIDAR, as well as boundary layer heights obtained from ERA5 dataset (white dashed line) and vertical potential temperature profiles (white solid line) measured by UAV on July 9th, 2018.

aerosols within the boundary layer, so the aerosol concentrations within the boundary layer decreased. Figure 5 shows the time series of range-corrected LIDAR signal and boundary layer heights retrieved from LIDAR as well as boundary layer height obtained from ERA5 dataset (white dash line) and potential temperature obtained from UAV measurements (white solid line) on July 12th, 2018. The reason for showing range-corrected LIDAR signal instead of backscatter coefficients is that low-level clouds prevented retrieving the backscatter coefficients from range-corrected LIDAR signal by the Klett-Fernald method. This figure also shows consistency in boundary layer heights among LIDAR, UAV, and ERA5. More interestingly, the cloud existed at the top of the boundary layer from 05:00 to 13:00 and the cloud base increased with boundary layer height as captured by the LIDAR measurements. The reason for the cloud existing on the top of the boundary layer is that the relative humidity has a maximum value at the top of the boundary layer in the well-mixing boundary layer and this high relative humidity ambient environment provided a good conditions for cloud formation. Figure S3 shows the correlation of boundary layer heights from LIDAR and radiosonde retrievals for both two days, which show a good correlation with a slope of 1.01 ± 0.24 and a Pearson correlation coefficient of 0.793.

A comparison of the vertical profile of aerosols from LIDAR and UAV measurements was conducted in the following steps. First, we used the temperature and pressure measured by UAV instead of an atmospheric model to calculate molecular backscat-

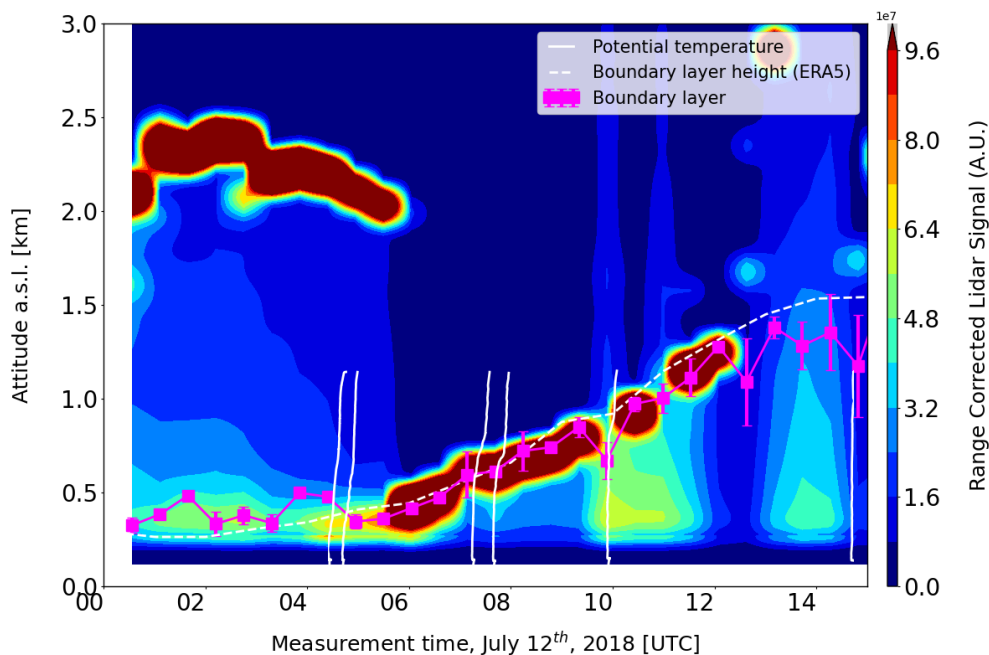


Figure 5. Time series of range corrected LIDAR signal and boundary layer height retrieved from scanning LIDAR (pink squares) as well as boundary layer heights obtained from ERA5 dataset (white dashed line) and vertical potential temperature profiles (white solid line) measured by UAV on July 12th, 2018.

ter coefficients, and these molecular backscatter profiles were used for LIDAR retrievals. Second, the backscatter coefficients at all observation angles were calculated using the Klett-Fernald method with reference values obtained from vertical profiles of the backscatter coefficients. Finally, Mie theory was used to calculate the aerosol backscatter coefficients based on size distributions measured by the UAV-borne OPC and the complex refractive index from a nearby sun photometer. As there are no dryer before OPC-N3 sampling and no temperature difference between sampling tube and ambient environment, the effect of relative humidity on aerosol sampling was not considered. Figure 6 shows the backscatter coefficients retrieved from LIDAR measurements and from Mie calculations based on size distributions measured by the OPC on the UAV. In this experiment, the LIDAR performed zenith scans using elevation angles from 90° to 5° with steps of 5° during the UAV flights. Consequently, we retrieve the backscatter coefficients for each observation angle and the average of these backscatter coefficients is shown as thick red line to compare with the UAV measurements. This figure shows that the vertical distribution of the aerosol particles in the well-mixed boundary layer is reflected well in both LIDAR and OPC measurements. Furthermore, the backscatter coefficients from UAV retrievals (green dashed line in figure 6) show the same aerosol mixing height and the same order of backscatter coefficients as LIDAR retrievals. The smaller backscatter coefficients calculated based on airborne OPC measurements may be related to an undercounting of the smaller particles as we have seen for ground based OPC measurements by the Fidas 200 instrument. The size distributions were corrected (black dashed line in figure 6) by the counting efficiency curve

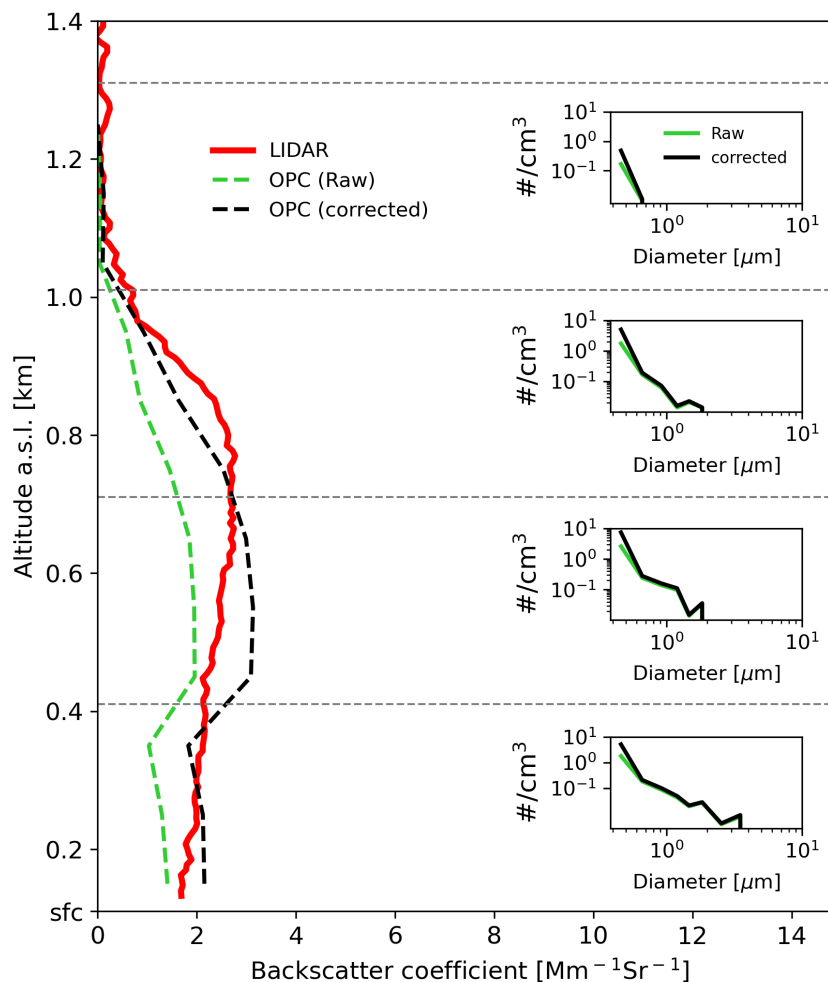


Figure 6. Vertical distribution of backscatter coefficients from LIDAR measurement (solid red line), as well as backscatter coefficients derived from UAV-based measurements for raw size distributions (dashed green line), and corrected particle size distributions (dashed black line) (inserts on the right) on July 9th, 2018. Note: The 'sfc' on the y-axis indicates ground surface level.

introduced in section 3.1. The backscatter coefficients from corrected size distributions were consistent with the lidar-derived backscatter coefficients. Although Fidas200 is a different OPC sensor as OPC-N3, the same undercounting phenomenon was observed for both sensors. Please note that the particle size is averaged over 300 m and the horizontal dashed lines represent these average altitude ranges. These vertical size distributions show that larger particles were detected only below 300 m above ground level.

12 UAV flights were conducted on July 9th and July 12th as shown in Table 1 to compare with LIDAR retrievals. Figure

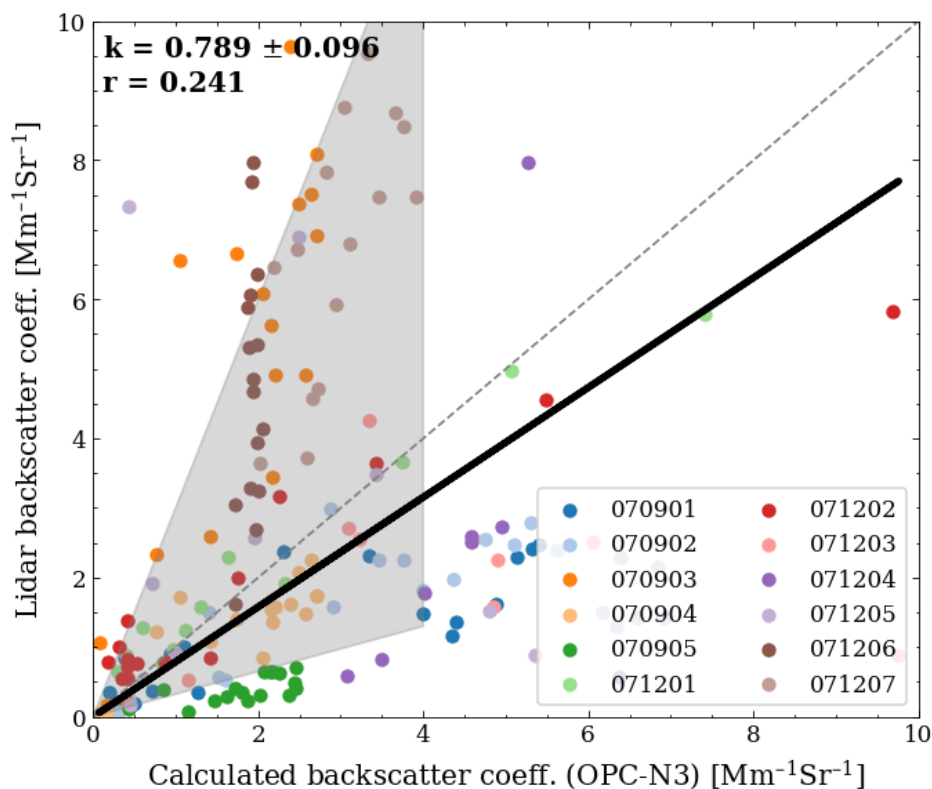


Figure 7. Correlation of backscatter coefficients retrieved from LIDAR measurement and modelled from Mie calculation based on aerosol size distribution measured by OPC-N3 on the UAV for all UAV flights on July 9th and July 12th, 2018. The different scatter point colours indicates different UAV flights. The thick black line is a linear fit to the data and the thin dashed line is the 1:1 line

7 shows the correlation of backscatter coefficients retrieved from LIDAR measurement and from Mie calculation based on aerosol size distributions measured by OPC-N3 on the UAV. The data from LIDAR and UAV was averaged into 60 m vertical bins to reduce the noise of the OPC-N3 measurement. The colours of the scatter points indicated different UAV flights. This figure shows that the backscatter coefficients retrieved from LIDAR correlated on average with the backscatter coefficients calculated from the OPC with a slope of 0.789 ± 0.096 and a Pearson correlation coefficient of 0.234. This figure also shows that 75% of data points are within the grey shaded area, which indicates that these data are within a factor of 3. However, in contrast to the ground level OPC measurements a dedicated correction of the low cost OPC data for potential sampling artefacts or undercounting was not possible. This figure also shows that the UAV measurements reflect the same aerosol mixing process within the boundary layer and the same order of magnitude of the backscatter coefficient. However, the backscatter coefficients retrieved from UAV-borne OPC in certain UAV flights still show a relatively large deviation from LIDAR retrievals in certain flights. One reason for these unstable observations is that the UAV cruising speed may affect aerosol sampling by the OPC-N3.



300 The sample was collected perpendicular to the flight's direction into the OPC, so we can expect size-dependent discrimination
of larger particles.

3.3 Comparison of LIDAR data with *in-situ* measurements onboard a balloon

A balloon which carried the COBALD sensor to measure backscatter coefficients *in-situ* was launched to an altitude of around
30 km on the night of July 12th, 2018 to validate LIDAR retrievals. The LIDAR did vertically pointed measurements with
305 an integration time of 60 s for each profile during the balloon launch. Figure 8a shows the range corrected LIDAR signal for
two hours of continuous measurement and the vertical trajectory of the balloon. As shown in this figure, the LIDAR signal
did not vary much in the first hour (the period was highlighted in this figure) while showing changes in the second half of the
experiment. Hence, we selected the first hour to compare with balloon measurements. Figure 8b shows the horizontal trajectory
of the radiosonde with the colour of the plot indicating the radiosonde altitude and the circle indicating the distance from the
310 LIDAR observation station. This figure shows that the horizontal displacement of the radiosonde is about 10 km when the
radiosonde reached an altitude of 10 km and this horizontal displacement may cause a difference in backscatter coefficients
between LIDAR and COBALD. For the LIDAR analysis in this experiment, the backscatter coefficients were retrieved from
elastic and Raman data with the vertical profiles of the molecular backscatter coefficient being calculated from temperature and
pressure measured by the balloon. The COBALD data analysis follows the procedure proposed by Brunamonti et al. (2021).
315 First, a wavelength extrapolation yielded the backscatter coefficient at a wavelength of 355 nm from COBALD measurement.
The Ångström exponent (AE) used for this wavelength conversion is measured by COBALD at two wavelengths (455 nm &
940 nm) and extended to the wavelength of 355 nm. Second, as the Field of View (FOV) of LIDAR and COBALD are different
(the FOV of COBALD is 6° whereas the FOV of LIDAR is 2.3 mrad), a FOV correction is necessary. The correction factors
are calculated based on Mie theory and are shown in Figure 2 in Brunamonti et al. (2021).
320 Figure 9 shows the backscatter coefficients from COBALD and LIDAR measurement for a LIDAR integration time of 1 hour.
These two profiles of backscatter coefficients from LIDAR are retrieved from elastic and Raman channel data respectively.

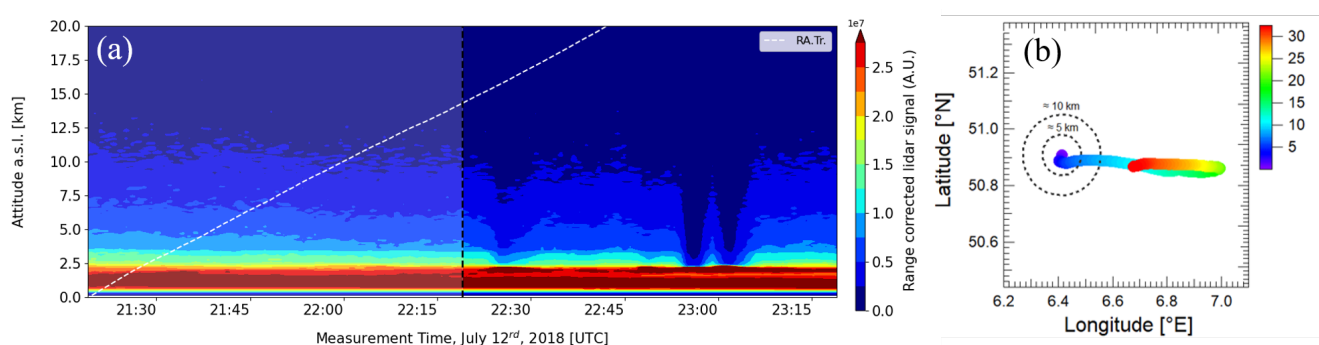


Figure 8. Time series of range corrected LIDAR signal and radiosonde vertical trajectory (white dash line) (a) and Horizontal displacement of the balloon during this experiment (b) on July 12th, 2018 at Jülich research center.

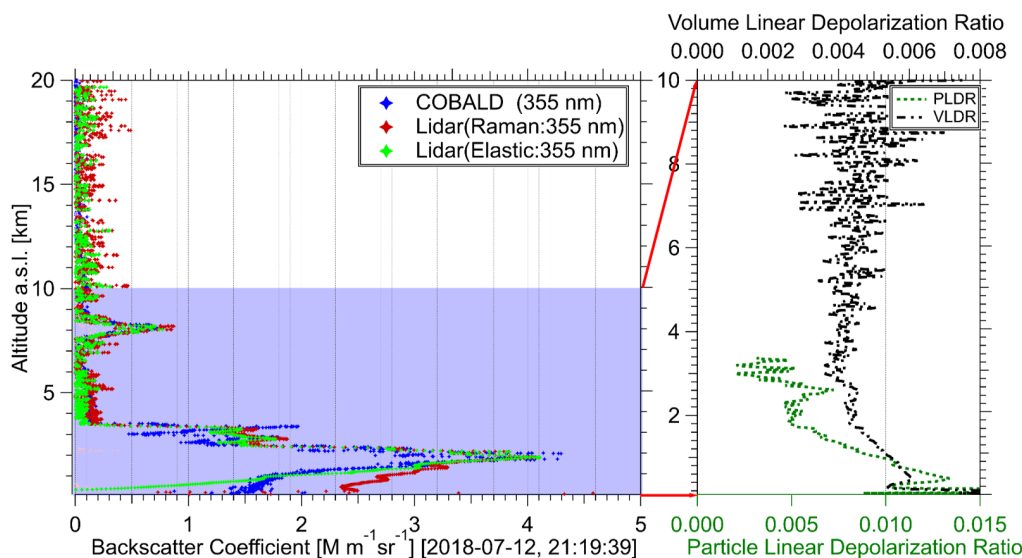


Figure 9. Backscatter coefficients measured by balloon-borne COBALD and LIDAR (left) as well as aerosol volume and particle depolarization ratio measured by LIDAR (right) on the night time of July 12th, 2018 at Jülich research center. (The integration time of the LIDAR data is 1 hour from 21:19 to 22:19.)

The retrieval of backscatter coefficients from elastic channel data remained with larger uncertainty due to the assumption of a LIDAR ratio in the Klett-Fernald method. Hence, it is more meaningful to compare backscatter coefficients from Raman data with those from COBALD measurements. In addition, the volume and particle depolarization ratios measured by LIDAR are shown on the right side of Figure 9. The low depolarization ratios support our assumption that the particles are spherical and that we can use Mie calculations for the FOV correction. This figure shows a good agreement in backscatter coefficients between LIDAR Raman data retrieval and COBALD measurement at an altitude above 2 km. However, there is a significant discrepancy at altitudes below 2 km.

The discrepancy of the backscatter coefficients between LIDAR retrievals and COBALD measurements at lower altitudes is due to the temporal evolution of aerosol particle concentrations in the boundary layer as can be seen from vertical profiles of backscatter coefficients with high temporal resolution in Figure S4. This figure shows profiles of backscatter coefficients retrieved from LIDAR Raman data with 5 - minute temporal resolution and backscatter coefficients measured by COBALD as well as the vertical balloon trajectory. This figure shows a good agreement in backscatter coefficients between COBALD measurement and LIDAR Raman data retrievals at the altitude of the balloon passing by. The backscatter values at the altitude of the balloon passing by are extracted as shown as the red line in Figure S4 to obtain merged Raman backscatter coefficients. The merged Raman backscatter coefficients and backscatter coefficients from COBALD measurements are shown on the left side of Figure 10, showing very good agreement of backscatter coefficients from LIDAR and COBALD measurements at all altitudes. The correlation between LIDAR merged Raman backscatter coefficients and COBALD backscatter coefficients is



shown on the right side of Figure 10, which shows these two backscatter coefficients are well correlated with a slope of 1.063 ± 0.016 and a Pearson correlation coefficient of 0.925. This consistency between LIDAR and COBALD sensor reflects a good data quality of both methods and proves that LIDAR can provide reliable and vertical profiles of aerosol particles with high spatial-temporal resolution.

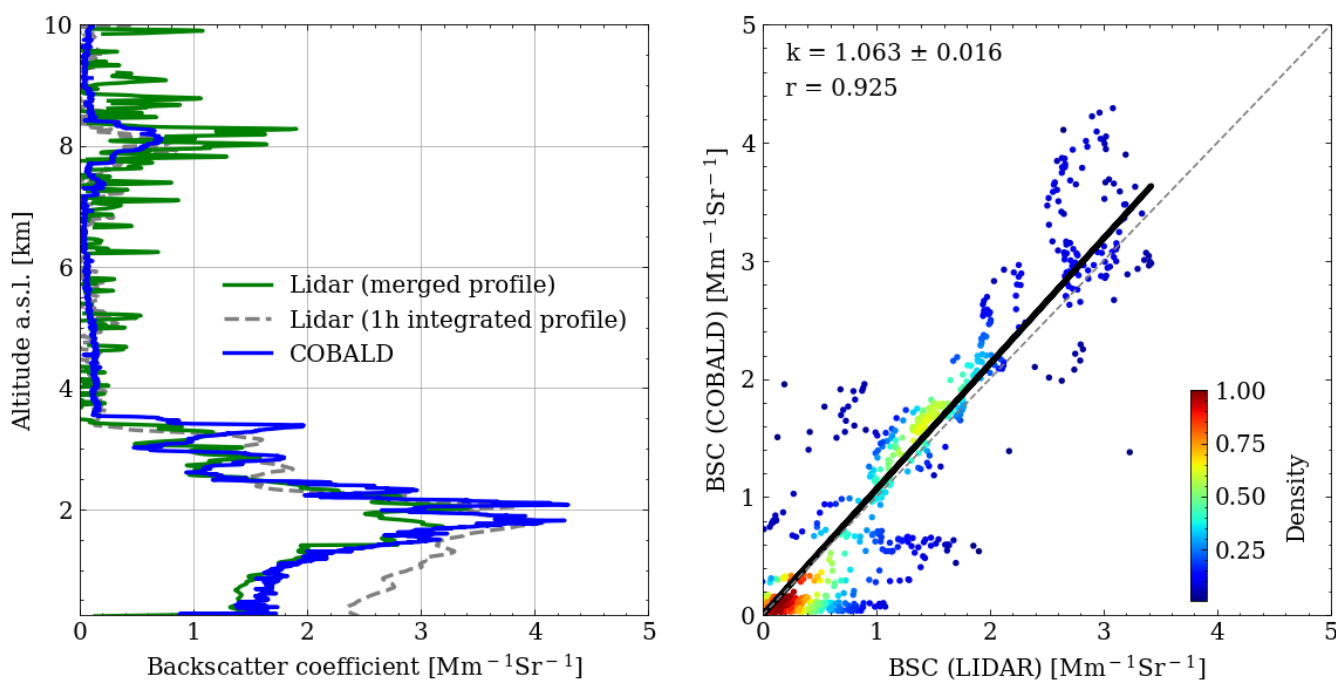


Figure 10. Profiles of backscatter coefficients from LIDAR for integration over 1 hour (grey dash line) and sliding 5-minute merged backscatter coefficients (green line) as well as the vertical profile of *in-situ* backscatter coefficient measured by balloon-borne COBALD (blue line) on July 12th, 2018 at the Jülich research center (left). Correlation between LIDAR merged backscatter coefficients and balloon-borne COBALD backscatter coefficients (right).

4 Conclusions

This paper presents results of aerosol spatial-temporal distribution and optical properties measured by a scanning aerosol LIDAR, a radiosonde with a backscatter sensor, an OPC-N3 on a UAV, and a comprehensive set of ground level *in-situ* measurements. Modern aerosol characterisation methods including remote sensing and *in-situ* methods helped us better understand the aerosol physical properties and build a bridge between remote sensing and these *in-situ* methods. This paper focuses on the comparison of aerosol measurement between LIDAR retrievals and *in-situ* measurements at ground level, in the troposphere, and in the stratosphere, thus validating LIDAR retrievals at all altitude levels.



The comparison of ground-level *in-situ* extinction coefficients with LIDAR-derived ones shows that Fidas200 underestimated particle number concentration by a factor of 2-10 at the diameter range between 0.25 μm and 0.5 μm , thus causing the total extinction calculated from this size distribution to be systematically lower than that from LIDAR retrievals by a factor of 4.70 ± 1.49 . The extinction coefficient calculated from the Fidas200 aerosol size distribution corrected by SMPS size distribution shows good agreement with LIDAR-derived extinction coefficient with a slope of 1.037 ± 0.015 and a Pearson correlation coefficient of 0.878. The comparison also shows that the undercounting of aerosol particles between 0.25 μm and 0.5 μm is the main reason for the large discrepancy between LIDAR retrieval and ground-level *in-situ* Fidas200 measurements. In addition, a comparison between LIDAR and UAV shows good agreement in boundary layer height measurements and both methods show a similar trend as the ERA5 boundary layer height evolution. The OPC-N3 aboard UAV shows a similar aerosol vertical distribution and comparable backscatter coefficients as LIDAR measurement. However, the backscatter coefficients calculated from OPC-N3 were unstable and large uncertainties still remained for different flights most likely due to the effect of UAV cruising on OPC-N3 sampling. Adapting the inlet design of the OPC may improve the data quality for future measurements. Finally, the backscatter from balloon-borne COBALD measurement shows very good agreement with the backscatter retrieved from LIDAR measurement if compared with 5-minute resolution LIDAR data with a slope of 1.063 ± 0.016 and a Pearson correlation coefficient of 0.925. This consistency between LIDAR and COBALD sensor validated our LIDAR retrievals and proves that LIDAR can provide reliable and high-resolution vertical profiles of aerosols. In conclusion, the retrievals from scanning aerosol LIDAR measurements show good agreement with *in-situ* measurements at all altitude levels and these LIDAR measurements can also be used as reference for other low cost *in-situ* measurements.

Code availability. The code used to analyse the LIDAR data is property of Raymetrics Inc, but we have shown that it gives the same results as the code "single calculus chain" (SCC) provided by EARLIENT https://www.earlinet.org/index.php?id=earlinet_homepage, last access: 14 February 2023 and public available. The Mie code used in this paper is available via github repository <https://github.com/jleinonen/pymiecoated>, last access: 14 February 2023.

Data availability. The LIDAR raw data and ground *in-situ* data are available via the open access data repository KITopen (link to be added). The UAV data and balloon data are available via the open access data repository Jülich DATA (link to be added).

Author contributions. CR, RT, CW, and HS performed the measurements and analyzed *in-situ* measurement data. HZ analysed the LIDAR remote sensing data. FGW post-processed the COBALD data. HZ wrote the manuscript with support from HS as well as contributions from all co-authors.

Competing interests. The authors declare that they have no conflict of interest.



Acknowledgements. Support by the staff of the Institute of Meteorology and Climate Research and the Institute of Energy and Climate
380 Research (FZJ), financial support by the project Modular Observation Solutions for Earth Systems (MOSES) of the Helmholtz Association
(HGF).



References

- Predicting forest fire in the Brazilian Amazon using MODIS imagery and artificial neural networks, *International Journal of Applied Earth Observation and Geoinformation*, 11, 265–272, <https://doi.org/10.1016/j.jag.2009.03.003>, 2009.
- 385 Alam, K., Trautmann, T., and Blaschke, T.: Aerosol optical properties and radiative forcing over mega-city Karachi, *Atmospheric Research*, 101, 773–782, <https://doi.org/10.1016/j.atmosres.2011.05.007>, international Conference on Nucleation and Atmospheric Aerosols (Part 2), 2011.
- Althausen, D., Müller, D., Ansmann, A., Wandinger, U., Hube, H., Clauer, E., and Zörner, S.: Scanning 6-wavelength 11-channel aerosol lidar, *Journal of Atmospheric and Oceanic Technology*, 17, 1469–1482, [https://doi.org/10.1175/1520-0426\(2000\)017<1469:SWCAL>2.0.CO;2](https://doi.org/10.1175/1520-0426(2000)017<1469:SWCAL>2.0.CO;2), 2000.
- 390 Anderson, T., Covert, D., Marshall, S., Laucks, M., Charlson, R., Waggoner, A., Ogren, J., Caldow, R., Holm, R., Quant, F., et al.: Performance characteristics of a high-sensitivity, three-wavelength, total scatter/backscatter nephelometer, *Journal of Atmospheric and Oceanic Technology*, 13, 967–986, [https://doi.org/10.1175/1520-0426\(1996\)013<0967:PCOAHS>2.0.CO;2](https://doi.org/10.1175/1520-0426(1996)013<0967:PCOAHS>2.0.CO;2), 1996.
- Ansmann, A., Wandinger, U., Riebesell, M., Weitkamp, C., and Michaelis, W.: Independent measurement of extinction and backscatter profiles in cirrus clouds by using a combined Raman elastic-backscatter lidar, *Applied optics*, 31, 7113–7131, <https://doi.org/10.1364/AO.31.007113>, 1992.
- 395 Avdikos, G.: Powerful Raman Lidar systems for atmospheric analysis and high-energy physics experiments, in: *EPJ Web of Conferences*, vol. 89, p. 04003, EDP Sciences, <https://doi.org/10.1051/epjconf/20158904003>, 2015.
- Bahreini, R., Jimenez, J. L., Wang, J., Flagan, R. C., Seinfeld, J. H., Jayne, J. T., and Worsnop, D. R.: Aircraft-based aerosol size and composition measurements during ACE-Asia using an Aerodyne aerosol mass spectrometer, *Journal of Geophysical Research: Atmospheres*, 108, <https://doi.org/10.1029/2002JD003226>, 2003.
- 400 Böckmann, C., Wandinger, U., Ansmann, A., Bösenberg, J., Amiridis, V., Boselli, A., Delaval, A., De Tomasi, F., Frioud, M., Grigorov, I. V., et al.: Aerosol lidar intercomparison in the framework of the EARLINET project. 2. Aerosol backscatter algorithms, *Applied Optics*, 43, 977–989, 2004.
- 405 Bohren, C. F. and Huffman, D. R.: *Absorption and scattering of light by small particles*, John Wiley & Sons, 2008.
- Brabec, M., Wienhold, F. G., Luo, B. P., Vömel, H., Immmler, F., Steiner, P., Hausammann, E., Weers, U., and Peter, T.: Particle backscatter and relative humidity measured across cirrus clouds and comparison with microphysical cirrus modelling, *Atmospheric Chemistry and Physics*, 12, 9135–9148, <https://doi.org/10.5194/acp-12-9135-2012>, 2012.
- Brunamonti, S., Jorge, T., Oelsner, P., Hanumanthu, S., Singh, B. B., Kumar, K. R., Sonbawne, S., Meier, S., Singh, D., Wienhold, F. G., Luo, B. P., Boettcher, M., Poltera, Y., Jauhiainen, H., Kayastha, R., Karmacharya, J., Dirksen, R., Naja, M., Rex, M., Fadnavis, S., and Peter, T.: Balloon-borne measurements of temperature, water vapor, ozone and aerosol backscatter on the southern slopes of the Himalayas during StratoClim 2016–2017, *Atmospheric Chemistry and Physics*, 18, 15 937–15 957, <https://doi.org/10.5194/acp-18-15937-2018>, 2018.
- 410 Brunamonti, S., Martucci, G., Romanens, G., Poltera, Y., Wienhold, F. G., Hervo, M., Haefele, A., and Navas-Guzmán, F.: Validation of aerosol backscatter profiles from Raman lidar and ceilometer using balloon-borne measurements, *Atmospheric Chemistry and Physics*, 21, 2267–2285, <https://doi.org/10.5194/acp-21-2267-2021>, 2021.
- 415 Ceolato, R. and Berg, M. J.: Aerosol light extinction and backscattering: A review with a lidar perspective, *Journal of Quantitative Spectroscopy and Radiative Transfer*, 262, 107 492, 2021.



- Cheng, K.-C., Acevedo-Bolton, V., Jiang, R.-T., Klepeis, N. E., Ott, W. R., Fringer, O. B., and Hildemann, L. M.: Modeling exposure close to
air pollution sources in naturally ventilated residences: Association of turbulent diffusion coefficient with air change rate, *Environmental
420 science & technology*, 45, 4016–4022, <https://doi.org/10.1021/es103080p>, 2011.
- Cirisan, A., Luo, B. P., Engel, I., Wienhold, F. G., Sprenger, M., Krieger, U. K., Weers, U., Romanens, G., Levrat, G., Jeannet, P., Ruffieux,
D., Philipona, R., Calpini, B., Spichtinger, P., and Peter, T.: Balloon-borne match measurements of midlatitude cirrus clouds, *Atmospheric
Chemistry and Physics*, 14, 7341–7365, <https://doi.org/10.5194/acp-14-7341-2014>, 2014.
- Drinovec, L., Močnik, G., Zotter, P., Prévôt, A. S. H., Ruckstuhl, C., Coz, E., Rupakheti, M., Sciare, J., Müller, T., Wiedensohler, A., and
425 Hansen, A. D. A.: The "dual-spot" Aethalometer: an improved measurement of aerosol black carbon with real-time loading compensation,
Atmospheric Measurement Techniques, 8, 1965–1979, <https://doi.org/10.5194/amt-8-1965-2015>, 2015.
- Düsing, S., Wehner, B., Seifert, P., Ansmann, A., Baars, H., Ditas, F., Henning, S., Ma, N., Poulain, L., Siebert, H., et al.: Helicopter-borne ob-
servations of the continental background aerosol in combination with remote sensing and ground-based measurements,
Atmospheric Chemistry and Physics, 18, 1263–1290, <https://doi.org/10.5194/acp-18-1263-2018>, 2018.
- 430 Engel, I., Luo, B. P., Khaykin, S. M., Wienhold, F. G., Vömel, H., Kivi, R., Hoyle, C. R., Grooß, J.-U., Pitts, M. C., and Peter, T.: Arctic strato-
spheric dehydration – Part 2: Microphysical modeling, *Atmospheric Chemistry and Physics*, 14, 3231–3246, <https://doi.org/10.5194/acp-14-3231-2014>, 2014.
- Fernald, F. G.: Analysis of atmospheric lidar observations: some comments, *Appl. Opt.*, 23, 652–653, <https://doi.org/10.1364/AO.23.000652>,
1984.
- 435 Ferrero, L., Ritter, C., Cappelletti, D., Moroni, B., Močnik, G., Mazzola, M., Lupi, A., Becagli, S., Traversi, R., Cataldi, M., et al.: Aerosol
optical properties in the Arctic: The role of aerosol chemistry and dust composition in a closure experiment between Lidar and tethered
balloon vertical profiles, *Science of the total environment*, 686, 452–467, <https://doi.org/10.1016/j.scitotenv.2019.05.399>, 2019.
- Filonchik, M. and Hurynovich, V.: Validation of MODIS aerosol products with AERONET measurements of different land cover types
in areas over Eastern Europe and China, *Journal of Geovisualization and Spatial Analysis*, 4, 1–11, <https://doi.org/10.1007/s41651-020-00052-9>, 2020.
- 440 Floutsi, A. A., Baars, H., Engelmann, R., Althausen, D., Ansmann, A., Bohlmann, S., Heese, B., Hofer, J., Kanitz, T., Haarig, M., Ohneiser,
K., Radenz, M., Seifert, P., Skupin, A., Yin, Z., Abdullaev, S. F., Komppula, M., Filioglou, M., Giannakaki, E., Stachlewska, I. S., Janicka,
L., Bortoli, D., Marinou, E., Amiridis, V., Gialitaki, A., Mamouri, R.-E., Barja, B., and Wandinger, U.: DeLiAn – a growing collection
of depolarization ratio, lidar ratio and Ångström exponent for different aerosol types and mixtures from ground-based lidar observations,
445 *Atmospheric Measurement Techniques Discussions*, 2022, 1–39, <https://doi.org/10.5194/amt-2022-306>, 2022.
- Fountoukis, C. and Nenes, A.: ISORROPIA II: a computationally efficient thermodynamic equilibrium model for
 K^+ – Ca^{2+} – Mg^{2+} – NH_4^+ – Na^+ – SO_4^{2-} – NO_3^- – Cl^- – H_2O aerosols, *Atmo-
spheric Chemistry and Physics*, 7, 4639–4659, <https://doi.org/10.5194/acp-7-4639-2007>, 2007.
- Freudenthaler, V.: About the effects of polarising optics on lidar signals and the $\Delta 90$ calibration, *Atmospheric Measurement Techniques*, 9,
450 4181–4255, <https://doi.org/10.5194/amt-9-4181-2016>, 2016.
- Ginoux, P., Prospero, J. M., Gill, T. E., Hsu, N. C., and Zhao, M.: Global-scale attribution of anthropogenic and natural dust sources and their
emission rates based on MODIS Deep Blue aerosol products, *Reviews of Geophysics*, 50, <https://doi.org/10.1029/2012RG000388>, 2012.
- Grythe, H., Ström, J., Krejci, R., Quinn, P., and Stohl, A.: A review of sea-spray aerosol source functions using a
large global set of sea salt aerosol concentration measurements, *Atmospheric Chemistry and Physics*, 14, 1277–1297,
455 <https://doi.org/10.1016/j.atmosres.2012.09.021>, 2014.



- Guimarães, P., Ye, J., Batista, C., Barbosa, R., Ribeiro, I., Medeiros, A., Souza, R., and Martin, S. T.: Vertical Profiles of Ozone Concentration Collected by an Unmanned Aerial Vehicle and the Mixing of the Nighttime Boundary Layer over an Amazonian Urban Area, *Atmosphere*, 10, <https://doi.org/10.3390/atmos10100599>, 2019.
- 460 Hamilton, F. W., Gregson, F. K., Arnold, D. T., Sheikh, S., Ward, K., Brown, J., Moran, E., White, C., Morley, A. J., Bzdek, B. R., et al.: Aerosol emission from the respiratory tract: an analysis of aerosol generation from oxygen delivery systems, *Thorax*, 77, 276–282, <https://doi.org/10.1136/thoraxjnl-2021-217577>, 2022.
- Hofer, J., Ansmann, A., Althausen, D., Engelmann, R., Baars, H., Fomba, K. W., Wandinger, U., Abdullaev, S. F., and Makhmudov, A. N.: Optical properties of Central Asian aerosol relevant for spaceborne lidar applications and aerosol typing at 355 and 532 nm, *Atmospheric Chemistry and Physics*, 20, 9265–9280, 2020.
- 465 Holben, B., Eck, T., Slutsker, I., Tanré, D., Buis, J., Setzer, A., Vermote, E., Reagan, J., Kaufman, Y., Nakajima, T., Lavenu, F., Jankowiak, I., and Smirnov, A.: AERONET—A Federated Instrument Network and Data Archive for Aerosol Characterization, *Remote Sensing of Environment*, 66, 1–16, [https://doi.org/10.1016/S0034-4257\(98\)00031-5](https://doi.org/10.1016/S0034-4257(98)00031-5), 1998.
- Huang, W., Saathoff, H., Shen, X., Ramisetty, R., Leisner, T., and Mohr, C.: Seasonal characteristics of organic aerosol chemical composition and volatility in Stuttgart, Germany, *Atmospheric Chemistry and Physics*, 19, 11 687–11 700, <https://doi.org/10.5194/acp-19-11687-2019>, 470 2019.
- Huesca, M., Litago, J., Palacios-Orueta, A., Montes, F., Sebastián-López, A., and Escribano, P.: Assessment of forest fire seasonality using MODIS fire potential: A time series approach, *Agricultural and Forest Meteorology*, 149, 1946–1955, <https://doi.org/10.1016/j.agrformet.2009.06.022>, special Section on Water and Carbon Dynamics in Selected Ecosystems in China, 2009.
- Jiang, F., Song, J., Bauer, J., Gao, L., Vallon, M., Gebhardt, R., Leisner, T., Norra, S., and Saathoff, H.: Chromophores and chemical 475 composition of brown carbon characterized at an urban kerbside by excitation–emission spectroscopy and mass spectrometry, *Atmospheric Chemistry and Physics*, 22, 14 971–14 986, <https://doi.org/10.5194/acp-22-14971-2022>, 2022.
- Kaufman, Y., Koren, I., Remer, L., Tanré, D., Ginoux, P., and Fan, S.: Dust transport and deposition observed from the Terra-Moderate Resolution Imaging Spectroradiometer (MODIS) spacecraft over the Atlantic Ocean, *Journal of Geophysical Research: Atmospheres*, 110, <https://doi.org/10.1029/2003JD004436>, 2005.
- 480 Khlebtsov, N. G., Melnikov, A. G., Bogatyrev, V. A., Dykman, L. A., Alekseeva, A. V., Trachuk, L. A., and Khlebtsov, B. N.: Can the Light Scattering Depolarization Ratio of Small Particles Be Greater Than 1/3?, *The Journal of Physical Chemistry B*, 109, 13 578–13 584, <https://doi.org/10.1021/jp0521095>, publisher: American Chemical Society, 2005.
- Klett, J. D.: Lidar inversion with variable backscatter/extinction ratios, *Appl. Opt.*, 24, 1638–1643, <https://doi.org/10.1364/AO.24.001638>, 1985.
- 485 Kotthaus, S., Bravo-Aranda, J. A., Collaud Coen, M., Guerrero-Rascado, J. L., Costa, M. J., Cimini, D., O’Connor, E. J., Hervo, M., Alados-Arboledas, L., Jiménez-Portaz, M., Mona, L., Ruffieux, D., Illingworth, A., and Haeffelin, M.: Atmospheric boundary layer height from ground-based remote sensing: a review of capabilities and limitations, *Atmospheric Measurement Techniques*, 16, 433–479, <https://doi.org/10.5194/amt-16-433-2023>, 2023.
- Leinonen, J.: Python code for calculating Mie scattering from single- and dual-layered spheres, <https://github.com/jleinonen/pymiecoated/>, 490 2016.
- Lesins, G., Chylek, P., and Lohmann, U.: A study of internal and external mixing scenarios and its effect on aerosol optical properties and direct radiative forcing, *Journal of Geophysical Research: Atmospheres*, 107, AAC–5, 2002.



- Li, H., Liu, B., Ma, X., Jin, S., Ma, Y., Zhao, Y., and Gong, W.: Evaluation of retrieval methods for planetary boundary layer height based on radiosonde data, *Atmospheric Measurement Techniques*, 14, 5977–5986, <https://doi.org/10.5194/amt-14-5977-2021>, 2021.
- 495 Li, Z., Guo, J., Ding, A., Liao, H., Liu, J., Sun, Y., Wang, T., Xue, H., Zhang, H., and Zhu, B.: Aerosol and boundary-layer interactions and impact on air quality, *National Science Review*, 4, 810–833, <https://doi.org/10.1093/nsr/nwx117>, 2017.
- Liu, C., Huang, J., Wang, Y., Tao, X., Hu, C., Deng, L., Xu, J., Xiao, H.-W., Luo, L., Xiao, H.-Y., et al.: Vertical distribution of PM_{2.5} and interactions with the atmospheric boundary layer during the development stage of a heavy haze pollution event, *Science of the Total Environment*, 704, 135–139, <https://doi.org/10.1016/j.scitotenv.2019.135329>, 2020.
- 500 Liu, C., Huang, J., Tao, X., Deng, L., Fang, X., Liu, Y., Luo, L., Zhang, Z., Xiao, H.-W., and Xiao, H.-Y.: An observational study of the boundary-layer entrainment and impact of aerosol radiative effect under aerosol-polluted conditions, *Atmospheric Research*, 250, 105–118, <https://doi.org/10.1016/j.atmosres.2020.105348>, 2021.
- Lolli, S., D’Adderio, L. P., Campbell, J. R., Sicard, M., Welton, E. J., Binci, A., Rea, A., Tokay, A., Comerón, A., Barragan, R., Baldasano, J. M., Gonzalez, S., Bech, J., Afflitto, N., Lewis, J. R., and Madonna, F.: Vertically Resolved Precipitation Intensity Retrieved through a Synergy between the Ground-Based NASA MPLNET Lidar Network Measurements, Surface Disdrometer Datasets and an Analytical Model Solution, *Remote Sensing*, 10, <https://doi.org/10.3390/rs10071102>, 2018.
- 505 Marinou, E., Amiridis, V., Biniotoglou, I., Tsikerdekis, A., Solomos, S., Proestakis, E., Konsta, D., Papagiannopoulos, N., Tsekeri, A., Vlastou, G., Zanis, P., Balis, D., Wandinger, U., and Ansmann, A.: Three-dimensional evolution of Saharan dust transport towards Europe based on a 9-year EARLINET-optimized CALIPSO dataset, *Atmospheric Chemistry and Physics*, 17, 5893–5919, <https://doi.org/10.5194/acp-17-5893-2017>, 2017.
- Matthais, V., Freudenthaler, V., Amodeo, A., Balin, I., Balis, D., Bösenberg, J., Chaikovsky, A., Chourdakis, G., Comeron, A., Delaval, A., et al.: Aerosol lidar intercomparison in the framework of the EARLINET project. 1. Instruments, *Applied Optics*, 43, 961–976, 2004.
- Matthias, V. and Bösenberg, J.: Aerosol climatology for the planetary boundary layer derived from regular lidar measurements, *Atmospheric Research*, 63, 221–245, 2002.
- 515 Mielonen, T., Arola, A., Komppula, M., Kukkonen, J., Koskinen, J., De Leeuw, G., and Lehtinen, K.: Comparison of CALIOP level 2 aerosol subtypes to aerosol types derived from AERONET inversion data, *Geophysical Research Letters*, 36, <https://doi.org/10.1029/2009GL039609>, 2009.
- More, S., Kumar, P. P., Gupta, P., Devara, P., and Aher, G.: Comparison of Aerosol Products Retrieved from AERONET, MICROTOPS and MODIS over a Tropical Urban City, Pune, India, *Aerosol and Air Quality Research*, 13, 107–121, <https://doi.org/10.4209/aaqr.2012.04.0102>, 2013.
- 520 Moroz, A.: Depolarization field of spheroidal particles, *JOSA B*, 26, 517–527, <https://doi.org/10.1364/JOSAB.26.000517>, publisher: Optica Publishing Group, 2009.
- Munchak, L. A., Levy, R. C., Mattoo, S., Remer, L. A., Holben, B. N., Schafer, J. S., Hostetler, C. A., and Ferrare, R. A.: MODIS 3 km aerosol product: applications over land in an urban/suburban region, *Atmospheric Measurement Techniques*, 6, 1747–1759, <https://doi.org/10.5194/amt-6-1747-2013>, 2013.
- 525 Pappalardo, G., Amodeo, A., Apituley, A., Comeron, A., Freudenthaler, V., Linné, H., Ansmann, A., Bösenberg, J., D’Amico, G., Mattis, I., Mona, L., Wandinger, U., Amiridis, V., Alados-Arboledas, L., Nicolae, D., and Wiegner, M.: EARLINET: towards an advanced sustainable European aerosol lidar network, *Atmospheric Measurement Techniques*, 7, 2389–2409, <https://doi.org/10.5194/amt-7-2389-2014>, 2014a.



- Pappalardo, G., Amodeo, A., Apituley, A., Comeron, A., Freudenthaler, V., Linné, H., Ansmann, A., Bösenberg, J., D'Amico, G., Mattis, I., et al.: EARLINET: towards an advanced sustainable European aerosol lidar network, *Atmospheric Measurement Techniques*, 7, 2389–2409, 2014b.
- Poreh, M. and Cermak, J.: Study of diffusion from a line source in a turbulent boundary layer, *International Journal of Heat and Mass Transfer*, 7, 1083–1095, [https://doi.org/10.1016/0017-9310\(64\)90032-8](https://doi.org/10.1016/0017-9310(64)90032-8), 1964.
- Prasad, A. K. and Singh, R. P.: Changes in aerosol parameters during major dust storm events (2001–2005) over the Indo-Gangetic Plains using AERONET and MODIS data, *Journal of Geophysical Research: Atmospheres*, 112, <https://doi.org/10.1029/2006JD007778>, 2007.
- Qin, W., Fang, H., Wang, L., Wei, J., Zhang, M., Su, X., Bilal, M., and Liang, X.: MODIS high-resolution MAIAC aerosol product: Global validation and analysis, *Atmospheric Environment*, 264, 118 684, <https://doi.org/10.1016/j.atmosenv.2021.118684>, 2021.
- Ramanathan, V., Crutzen, P. J., Kiehl, J., and Rosenfeld, D.: Aerosols, climate, and the hydrological cycle, *science*, 294, 2119–2124, <https://doi.org/10.1126/science.1064034>, 2001.
- 540 Raut, J.-C. and Chazette, P.: Vertical profiles of urban aerosol complex refractive index in the frame of ESQUIF airborne measurements, *Atmospheric Chemistry and Physics*, 8, 901–919, <https://doi.org/10.5194/acp-8-901-2008>, 2008.
- Reineman, B. D., Lenain, L., and Melville, W. K.: The use of ship-launched fixed-wing UAVs for measuring the marine atmospheric boundary layer and ocean surface processes, *Journal of Atmospheric and Oceanic Technology*, 33, 2029–2052, <https://doi.org/10.1175/JTECH-D-15-0019.1>, 2016.
- 545 Romshoo, B., Müller, T., Pfeifer, S., Saturno, J., Nowak, A., Ciupek, K., Quincey, P., and Wiedensohler, A.: Optical properties of coated black carbon aggregates: numerical simulations, radiative forcing estimates, and size-resolved parameterization scheme, *Atmospheric Chemistry and Physics*, 21, 12 989–13 010, <https://doi.org/10.5194/acp-21-12989-2021>, 2021.
- Rosen, J. M. and Kjome, N. T.: Backscattersonde: a new instrument for atmospheric aerosol research, *Appl. Opt.*, 30, 1552–1561, <https://doi.org/10.1364/AO.30.001552>, 1991.
- 550 Salehi, M., Masoumi, A., and Moradhaseli, R.: A study on the vertical distribution of dust transported from the Tigris–Euphrates basin to the Northwest Iran Plateau based on CALIOP/CALIPSO data, *Atmospheric Pollution Research*, 12, 101 228, <https://doi.org/10.1016/j.apr.2021.101228>, 2021.
- Seidel, D. J., Ao, C. O., and Li, K.: Estimating climatological planetary boundary layer heights from radiosonde observations: Comparison of methods and uncertainty analysis, *Journal of Geophysical Research: Atmospheres*, 115, <https://doi.org/10.1029/2009JD013680>, 2010.
- 555 Smit, H. G., Straeter, W., Johnson, B. J., Oltmans, S. J., Davies, J., Tarasick, D. W., Hoegger, B., Stubi, R., Schmidlin, F. J., Northam, T., et al.: Assessment of the performance of ECC-ozonesondes under quasi-flight conditions in the environmental simulation chamber: Insights from the Juelich Ozone Sonde Intercomparison Experiment (JOSIE), *Journal of Geophysical Research: Atmospheres*, 112, <https://doi.org/10.1029/2006JD007308>, 2007.
- Spiess, T., Bange, J., Buschmann, M., and Vorsmann, P.: First application of the meteorological Mini-UAV'M2AV', *Meteorologische Zeitschrift*, 16, 159–170, <https://doi.org/10.1127/0941-2948/2007/0195>, 2007.
- 560 Stocker, T.: *Climate change 2013: the physical science basis: Working Group I contribution to the Fifth assessment report of the Intergovernmental Panel on Climate Change*, Cambridge university press, 2014.
- Tegen, I. and Schepanski, K.: Climate feedback on aerosol emission and atmospheric concentrations, *Current Climate Change Reports*, 4, 1–10, <https://doi.org/10.1007/s40641-018-0086-1>, 2018.



- 565 Vernier, J.-P., Fairlie, T. D., Natarajan, M., Wienhold, F. G., Bian, J., Martinsson, B. G., Crumeyrolle, S., Thomason, L. W., and Bedka, K. M.: Increase in upper tropospheric and lower stratospheric aerosol levels and its potential connection with Asian pollution, *Journal of Geophysical Research: Atmospheres*, 120, 1608–1619, <https://doi.org/10.1002/2014JD022372>, 2015.
- Vernier, J.-P., Fairlie, T., Deshler, T., Ratnam, M. V., Gadhavi, H., Kumar, B., Natarajan, M., Pandit, A., Raj, S. A., Kumar, A. H., et al.: BATAL: The balloon measurement campaigns of the Asian tropopause aerosol layer, *Bulletin of the American Meteorological Society*, 570 99, 955–973, <https://doi.org/10.1175/BAMS-D-17-0014.1>, 2018.
- Vömel, H., David, D., and Smith, K.: Accuracy of tropospheric and stratospheric water vapor measurements by the cryogenic frost point hygrometer: Instrumental details and observations, *Journal of Geophysical Research: Atmospheres*, 112, <https://doi.org/10.1029/2006JD007224>, 2007.
- Vömel, H., Naebert, T., Dirksen, R., and Sommer, M.: An update on the uncertainties of water vapor measurements using cryogenic frost 575 point hygrometers, *Atmospheric Measurement Techniques*, 9, 3755–3768, <https://doi.org/10.5194/amt-9-3755-2016>, 2016.
- Wandinger, U. and Ansmann, A.: Experimental determination of the lidar overlap profile with Raman lidar, *Appl. Opt.*, 41, 511–514, <https://doi.org/10.1364/AO.41.000511>, 2002.
- Wang, X., Bi, L., Han, W., and Zhang, X.: Single-Scattering Properties of Encapsulated Fractal Black Carbon Particles Computed Using the Invariant Imbedding T-Matrix Method and Deep Learning Approaches, *Journal of Geophysical Research: Atmospheres*, 128, 580 e2023JD039568, <https://doi.org/10.1029/2023JD039568>, eprint: <https://onlinelibrary.wiley.com/doi/pdf/10.1029/2023JD039568>, 2023.
- Wang, Z., Liu, C., Hu, Q., Dong, Y., Liu, H., Xing, C., and Tan, W.: Quantify the Contribution of Dust and Anthropogenic Sources to Aerosols in North China by Lidar and Validated with CALIPSO, *Remote Sensing*, 13, <https://doi.org/10.3390/rs13091811>, 2021.
- Welton, E. J., Campbell, J. R., Berkoff, T. A., Valencia, S., Spinhirne, J. D., Holben, B., Tsay, S.-C., and Schmid, B.: The NASA Micro-Pulse Lidar Network (MPLNET): an overview and recent results, *Opt. Pur. Apl*, 39, 67–74, 2006.
- 585 Winker, D. M., Vaughan, M. A., Omar, A., Hu, Y., Powell, K. A., Liu, Z., Hunt, W. H., and Young, S. A.: Overview of the CALIPSO mission and CALIOP data processing algorithms, *Journal of Atmospheric and Oceanic Technology*, 26, 2310–2323, <https://doi.org/10.1175/2009JTECHA1281.1>, 2009.
- Xiafukaiti, A., Lagrosas, N., Ong, P. M., Saitoh, N., Shiina, T., and Kuze, H.: Comparison of aerosol properties derived from sampling and near-horizontal lidar measurements using mie scattering theory, *Applied Optics*, 59, 8014–8022, <https://doi.org/10.1364/AO.398673>, 590 2020.
- Xiang, Y., Zhang, T., Liu, J., Lv, L., Dong, Y., and Chen, Z.: Atmosphere boundary layer height and its effect on air pollutants in Beijing during winter heavy pollution, *Atmospheric Research*, 215, 305–316, <https://doi.org/https://doi.org/10.1016/j.atmosres.2018.09.014>, 2019.
- Xue, Q., Nie, W., Guo, L., Liu, Q., Hua, Y., Sun, N., Liu, C., and Niu, W.: Determining the optimal airflow rate to minimize air pollution in 595 tunnels, *Process Safety and Environmental Protection*, 157, 115–130, <https://doi.org/10.1016/j.psep.2021.10.039>, 2022.
- Yao, Y., Curtis, J. H., Ching, J., Zheng, Z., and Riemer, N.: Quantifying the effects of mixing state on aerosol optical properties, *Atmospheric Chemistry and Physics*, 22, 9265–9282, <https://doi.org/10.5194/acp-22-9265-2022>, 2022.
- Zarco-Tejada, P., González-Dugo, V., and Berni, J.: Fluorescence, temperature and narrow-band indices acquired from a UAV platform for water stress detection using a micro-hyperspectral imager and a thermal camera, *Remote Sensing of Environment*, 117, 322–337, 600 <https://doi.org/https://doi.org/10.1016/j.rse.2011.10.007>, *remote Sensing of Urban Environments*, 2012.

<https://doi.org/10.5194/ar-2024-3>

Preprint. Discussion started: 29 January 2024

© Author(s) 2024. CC BY 4.0 License.



Zhang, H., Wagner, F., Saathoff, H., Vogel, H., Hoshyaripour, G., Bachmann, V., Förstner, J., and Leisner, T.: Comparison of Scanning LiDAR with Other Remote Sensing Measurements and Transport Model Predictions for a Saharan Dust Case, *Remote Sensing*, 14, <https://doi.org/10.3390/rs14071693>, 2022.

605 Zhang, M., Tian, P., Zeng, H., Wang, L., Liang, J., Cao, X., and Zhang, L.: A comparison of wintertime atmospheric boundary layer heights determined by tethered balloon soundings and lidar at the site of SACOL, *Remote Sensing*, 13, 1781, <https://doi.org/10.3390/rs13091781>, 2021.

Zhen, Z., Jiang, S., and Ma, K.: Automatic carrier landing control for unmanned aerial vehicles based on preview control and particle filtering, *Aerospace Science and Technology*, 81, 99–107, <https://doi.org/10.1016/j.ast.2018.07.039>, 2018.